ACS APPLIED MATERIALS & INTERFACES

Research Article

www.acsami.org

Hydrophobic Meshes for Oil Spill Recovery Devices

Da Deng,[†,‡,§] Daniel P. Prendergast,[†,§] John MacFarlane,[†] Roberto Bagatin,[⊥] Francesco Stellacci,[#] and Philip M. Gschwend*[,†]

[†]Department of Civil and Environmental Engineering, Massachusetts Institute of Technology, Cambridge, Massachusetts 02139, United States

[‡]Department of Chemical Engineering and Materials Science, Wayne State University, Detroit, Michigan 48202, United States

[⊥]Research Centre for Non-Conventional Energy, Istituto Eni Donegani Environmental Technologies, Via Fauser 4, I-28100 Novara, Italy

[#]Institute of Materials, École Polytechnique Fédérale de Lausanne (EPFL), Lausanne CH-1015, Switzerland

Supporting Information

ABSTRACT: Widespread use of petrochemicals often leads to accidental releases in aquatic environments, occasionally with disastrous results. We have developed a hydrophobic and oleophilic mesh that separates oil from water continuously in situ via capillary action, providing a means of recovering spilt oil from surface waters. Steel mesh is dip-coated in a xylene solution of low-density polyethylene, creating a hydrophobic surface with tunable roughness and opening size. The hydrophobic mesh allows oil to pass through the openings while preventing the concomitant passage of water. A bench-top prototype demonstrated the efficacy of such an oil recovery device and allowed us to quantify the factors governing the ability of the mesh to separate oil and water. Preliminary data analysis suggested that the oleophilic openings behave somewhat like capillary tubes: the oil flux is inversely proportional to oil viscosity, and directly proportional to the size of the mesh openings. An unpinned meniscus model was found to predict the water intrusion pressure successfully, which increased as the opening size decreased. The trade-off between water intrusion and oil flow rate suggests an optimal pore size for given oil properties and sea conditions.

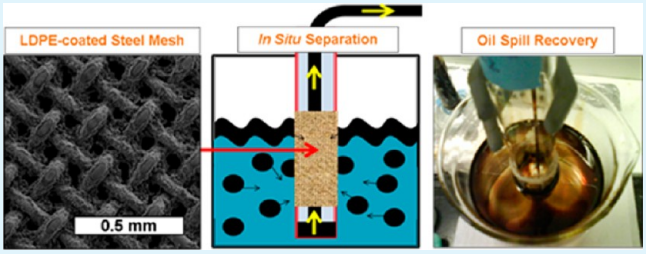

KEYWORDS: *low-density polyethylene (LDPE), separation, oil spill remediation, functionalized mesh, hydrophobic, oleophilic*

INTRODUCTION

All too commonly, human activities pollute aquatic environments with petroleum products from a variety of sources, including extraction wells, tankers, storage facilities, and refineries.[1] An extreme example is the 2010 Deepwater Horizon incident in the Gulf of Mexico, which released an estimated 4.1 million barrels of crude oil from approximately 66 km off the Louisiana shore.[2] The cost of the oil spill, including the damage to the coastal ecosystem and the loss of an entire fishing and tourism season, is still being tabulated. The failure to prevent crude oil from reaching sensitive areas increased damages, drew widespread public attention, and highlighted the need for new technological approaches to oil spill remediation.

The current technologies for handling oil spills include the use of skimmers, booms, in situ burning, sorbents, dispersants, and biodegradation.[3] These approaches vary in expense and effectiveness, and are focused on cleanup; only skimming and some sorbents are designed to recover the spilled oil. Mechanically driven skimmers utilize differences in density or wettability to separate the oil and water, but can only recover oil near the deployment vessel.[4] Sorbents can be spread over a large area, but have a finite capacity (polypropylene foams, the most common, absorb about 10 g of oil per gram of sorbent[5]) and must be collected after deployment. Safely handling the oil-soaked sorbent waste is challenging, as is recovering the absorbed oil.[4] These current limitations provide motivation for developing new oil spill recovery technologies.

An emerging approach to oil-water separations is the use of inexpensive, durable substrates with selectively wetting surfaces. In 2004, Feng et al.[6] coated a stainless steel mesh by spraying it with a polytetrafluoroethylene (PTFE) emulsion. The PTFE-coated mesh resisted wetting by water, but was completely wetted by nonpolar, low surface energy oils, making it superhydrophobic (water contact angle >150°) and oleophilic. A falling oil droplet was observed to rapidly pass through the mesh, which led to the conclusion that separation of oil and water using a selectively wetting mesh was feasible. Numerous separations have since been performed using metallic meshes whose surfaces have been functionalized to be hydrophobic and oleophilic. Fabrication methods include electrospinning or

Received: October 15, 2012
Accepted: January 16, 2013
Published: January 16, 2013

airbrushing polymer coatings,[7,8] inducing the growth of carbon nanotubes,[9,10] chemical etching,[11,12] growing fluorinated zinc oxide crystals,[13] and self-assembly of long-chain fatty acids.[14] Additionally, hydrophilic/oleophobic metallic meshes can separate oil and water by allowing the passage of water while preventing the flow of oil; such surfaces have been created by photoinitiated polymerization of hydrogel coatings,[15] solution grafting of perfluorinated polyethylene glycol surfactants[16] and spray coating nanoparticle−polymer suspensions.[17] This technique of functionalizing surfaces has also been extended to sorbents: Yuan et al.[18] coated a paperlike nanowire substrate with polydimethyl siloxane (PDMS). The coating both enhanced its hydrophobicity and markedly improved its ability to selectively absorb oil, even in the presence of large water quantities. Unfortunately, none of the above methods create a surface that is clearly both durable and economic to produce. In addition, quantitative analysis of the separation capabilities of the functionalized meshes has been limited.[19]

Herein, we report the successful fabrication of simple devices that: (1) recover oil floating on water at a rapid rate, (2) continuously separate oil and water without energy input, (3) are durable and reusable, and (4) are inexpensive to produce. Stainless steel meshes were dip-coated in xylene solutions of low-density polyethylene, giving them a hydrophobic and oleophilic surface while retaining the excellent mechanical properties of the underlying steel. The meshes were characterized by pore size and static contact angle, and they were integrated into a collection apparatus that successfully separated oil and water. In contrast to typical oil recovery techniques, our devices separate continuously via capillary action; oil only needs to be pumped away from the inside to perpetuate the process. Furthermore, this work quantifies the effects of coating roughness, pore size, and oil viscosity on the oil recovery rate and examines the water breakthrough pressures. The results provide a basis for the rational design and implementation of these devices in future oil spills.

MATERIALS AND METHODS

Materials. All our materials were used as received. Low-density polyethylene (LDPE) was obtained as pellets from Aldrich and had a melt flow index of 2.8 g min^{-1} at 190°. Woven stainless steel (304) meshes were obtained from McMaster-Carr with three opening sizes: 100, 220, and 1500 μm. All meshes were cleaned three times in an ultrasonic bath with a 50:50 ethanol:water solution for 5 min before use. ACS reagent-grade mixed-isomer xylenes were obtained from Sigma-Aldrich. Southern Louisiana crude oil was obtained from John Farrington of the Woods Hole Oceanographic Institute, while the other oils (castor, olive, and canola) were obtained from grocery stores. This set of oils reflects a broad range of viscosities encompassing those found for many crude oils (Table 1). The oil viscosities were measured in accordance with ASTM D-1545, and the surface tensions were measured using the capillary rise technique. Seawater was collected from the Port of Christopher Columbus Waterfront Park in Boston, MA.

Table 1. Physical Properties of Oils Tested with Bench-Top Oil−Water Separation Device

sample	surface tension[a] (dyn/cm)	viscosity[a] (cP)
canola oil	30.9 ± 0.7	73 ± 9
olive oil	30.2 ± 0.9	75 ± 9
castor oil	31.0 ± 0.7	780 ± 13
Southern Louisiana crude oil	28.8 ± 0.6	64 ± 9

[a]Measured at the experimental temperatures: 23 ± 1°C.

LDPE-Coated Mesh Preparation. First, the desired mass of LDPE was dissolved in the mixed-isomer xylenes at 110 °C while stirring. Concentrations of LDPE in xylene used in these experiments were limited to 15, 30, and 60 mg mL^{-1}. Then, a sample of the woven stainless steel mesh was soaked in the dissolved LDPE solution for 30 min to enable adhering air bubbles to escape. Subsequently, the mesh was removed fully wetted, kept in a horizontal position, and air-dried in a fume hood at room temperature on a wire scaffold. After air-drying for 30 min, the coated mesh was heated in a ventilated oven at 70 °C overnight.

Characterization of Meshes Using Optical Microscopy. Physical dimensions of the coated and uncoated meshes were measured using an inverted optical microscope (TE2000; Nikon). First, the areas of a large sampling of openings for each mesh-coating combination were measured and the mean area was calculated. Then, this mean area was used to calculate an effective pore radius r of a circle with equivalent area. The corresponding effective coated wire radius R was calculated by halving the width of an uncoated mesh opening, subtracting the effective pore radius, and adding the radius of the uncoated wire. An exception was made for meshes coated with a 15 mg mL^{-1} LDPE-xylene solution, since using this method would result in an effective coated wire radius smaller than the radius of an uncoated wire. In that case, the coated wire radius R was measured directly. A summary of these coated-mesh properties can be found in Table 2.

Contact Angle Measurements. Water contact angle measurements were made using 10 μL drops of distilled water at three different spots on each sample. Drop images were captured using a digital SLR camera (EOS Rebel XSi; Canon) fitted with a macro lens (EF 50 mm f/2.5 Compact Macro). The contact angle was determined from image data using software developed by Stalder et al.[20] The software uses a low-bond axisymmetric drop shape analysis (LBADSA) technique to fit the axisymmetric Young−Laplace equation to the shape of the drop. All measurements were taken three times, and reproducible to less than ±3°.

AFM Roughness Measurements. The roughness of a 10 μm by 10 μm area of the coated meshes was determined by probing the surface topography using an atomic force microscope (D3100, Nanoscope IIIa controller; Veeco/Digital Instruments, Santa Barbara, CA, USA). Because of the inherent curvature of the woven wire substrate, and the large size of the LDPE surface microstructures (commonly greater than 5 μm), the roughness ratio (ratio of the actual surface area to the projected surface area) could only be calculated for the most raised portion of the wires, which were relatively uncoated compared to the remainder of the mesh.

SEM Images. The micro- and nanoscale morphology of the LDPE coating was revealed using a field emission scanning electron microscope (SEM, JEOL) operating at 15 kV. Before FESEM observations, the samples were coated with gold to improve their surface conductivity by a gold sputter (EffaCoater) at 30 mA for 30 seconds in vacuum.

Crystallinity Measurements. The crystallinity of the LDPE coating was assessed using a power compensated differential scanning calorimeter (Diamond; Perkin Elmer) to measure the enthalpy of fusion. The temperature program consisted of: (1) ramp from 50 to 80 °C at 20 °C/min; (3) isothermal hold for 1 min at 80°C; (4) ramp to 150 °C at 20 °C/min; (5) isothermal hold at 50 °C for 1 min; (6) cool to 50 °C at 20°C/min. Reported values are calculated after subtracting a background uncoated mesh sample.

Breakthrough Pressure of Water. The depth at which the hydrostatic water pressure overcomes the capillary pressure within the mesh openings is the maximum operation depth for a given mesh. To test this, we coated a sample of each mesh size in a 60 mg mL^{-1} LDPE-xylene solution as described above. Then, each mesh was affixed to the end of a glass tube using adhesive and slowly lowered vertically into a clear tank of water. The shallowest depth at which water percolation occurred was recorded, while taking care to ensure that it did not originate from leaks around the adhesive seal.

Oil Spill Recovery. Experimental testing was performed in order to quantitatively assess the ability of the mesh to continuously recover

Table 2. Dimensions of Coated and Uncoated Meshes

approximate uncoated mesh opening size (μm)	coating concentration (mg/mL)	mean opening area of coated mesh (μm^2)	mean effective pore radius (μm)	effective coated wire radius (μm)
100	uncoated	9030 ± 480	95.0 ± 4.2[a]	58.3 ± 4.2[b]
	15 ± 1	7840 ± 510	50.0 ± 1.6	63.2 ± 4.2[b]
	30 ± 2	4600 ± 1100	38.2 ± 4.4	67 ± 11
	60 ± 4	150 ± 160	6.9 ± 3.9	99 ± 10
220	uncoated	35000 ± 1100	187 ± 4[a]	128 ± 4[b]
	15 ± 1	33000 ± 780	103 ± 1	132 ± 4[b]
	30 ± 2	21700 ± 980	83.0 ± 1.9	139 ± 8
	60 ± 4	9300 ± 1200	54.5 ± 3.4	167 ± 9
1500	uncoated	910000 ± 14000	954 ± 4[a]	185 ± 4[b]
	15 ± 1	908000 ± 14000	538 ± 4	188 ± 4[b]
	30 ± 2	726000 ± 13000	481 ± 4	206 ± 10
	60 ± 4	459000 ± 10000	382 ± 4	280 ± 10

[a]Actual opening width. [b]Actual wire radius.

four different types of oils (canola, olive, castor, and Southern Louisiana crude oil) from atop a pool of water. The mesh was mounted on the sides of a glass test tube (1″ OD) so as to cover "windows" cut in the side of the tube. The test tube was then immersed in a beaker with 400 mL of distilled water beneath a 25 mL layer of oil (0.5 cm thick) such that the mesh window was in contact with the oil layer (Figure 1). The oil immediately flowed through the

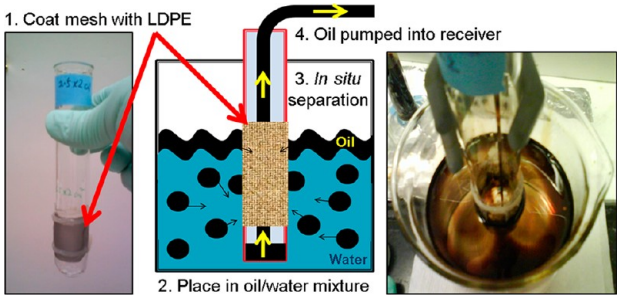

Figure 1. Center: illustration showing the integrated collection system recovering oil; blue represents seawater, black represents a crude oil spill. Left: photo of the test tube with windows cut in its side covered with a LDPE-coated mesh. This tube was lowered into beakers with floating oil. The oil passed through the mesh and was continuously pumped to an external reservoir. Right: photo showing the system during operation. Oil removal occurred on the sides of the device with mesh (left and right in the photo), but not elsewhere (e.g., bottom of photo).

mesh windows and pooled at the bottom of the test tube from which it was continuously pumped and collected in a separate graduated cylinder. The recovered volume was noted as a function of time. The first series of recovery experiments used the same 220 μm swatch of mesh coated in 60 mg mL^{-1} solution of LDPE-xylene while varying the oil. The mesh was rinsed with dichloromethane and air-dried between experiments. The second series of experiments used seawater and a single oil, Southern Louisiana crude, while varying the mesh size. Each mesh had been coated in a 60 mg mL^{-1} LDPE-xylene solution.

Determination of the Permeate Water Content. After each oil recovery experiment, an aliquot of oil permeate was immediately collected, sealed within a pre-weighed wide glass vial, and weighed again. The vial was later opened, sealed within a larger container containing anhydrous calcium sulfate, and kept at 60 °C for no less than 3 h. After cooling, the water content was determined gravimetrically from both the mass lost by the sample, and the mass gained by the desiccant. The detection limit for this method was determined to be 1% water by mass, based on error using external standards.

RESULTS AND DISCUSSION

Properties of the LDPE Coatings on Stainless Steel Meshes. The successful coating of LDPE on stainless steel mesh was characterized by optical microscopy and scanning electron microscopy (SEM). It was found that the thickness of the LDPE coating on the stainless steel mesh could be easily controlled by adjusting the initial dissolved concentration of LDPE in xylene (Figure 2). Compared to the wire diameter of

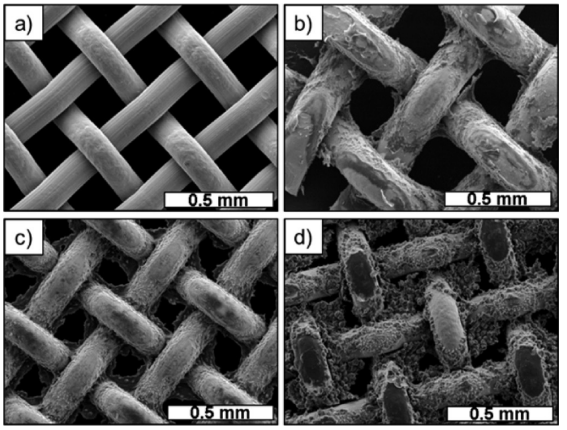

Figure 2. SEM micrographs of various coating concentrations (mg LDPE/mL xylene) on the 220 μm stainless steel mesh. The mesh was dipped into coating concentrations of: (a) uncoated mesh, (b) 15 mg mL^{-1}, (c) 30 mg mL^{-1}, and (d) 60 mg mL^{-1}.

the bare mesh (Figure 2a), the 15 mg mL^{-1} LDPE-xylene solution only increased the wire diameter by about 10% (Figure 2b) with a flaky coating, and tended to accrue in the narrower spaces within the weave. When the concentration was increased to 30 mg mL^{-1}, a significant increase in the amount of LDPE coated on the mesh was observed (Figure 2c). The SEM image indicates that the LDPE forms a thin film in the interstitial opening of the mesh, coplanar with the mesh orientation. In addition, the wires become more thickly coated with a rougher surface, again favoring the confined portions of the weave. These microstructures became even more obvious when the highest concentration of 60 mg mL^{-1} was used (Figure 2d). The LDPE coated on the mesh almost filled the 220 μm grid space between wires with highly irregular formations, whereas the most raised portions of the wires remained only lightly coated.

dx.doi.org/10.1021/am302338x | ACS Appl. Mater. Interfaces 2013, 5, 774−781

The same method was used to coat steel meshes with larger and smaller openings (Figure 3). The 100 μm mesh had a much more complete coating, including most of the raised portions of the wires (Figure 3a). The mesh openings were nearly completely closed off, with rough, jagged edges (Figure 3c). In contrast, the larger 1500 μm mesh had most of the LDPE concentrated in the corners or edges of the grid, creating "star-shaped" pores (Figure 3b, d). However, all meshes coated at this high concentration showcased similar surface morphologies, with microstructures particularly prominent on the interstitial LDPE. Additional optical microscopy (see the Supporting Information) suggests that the LDPE coating exhibits similar morphology for a given concentration, regardless of the size of the mesh opening.

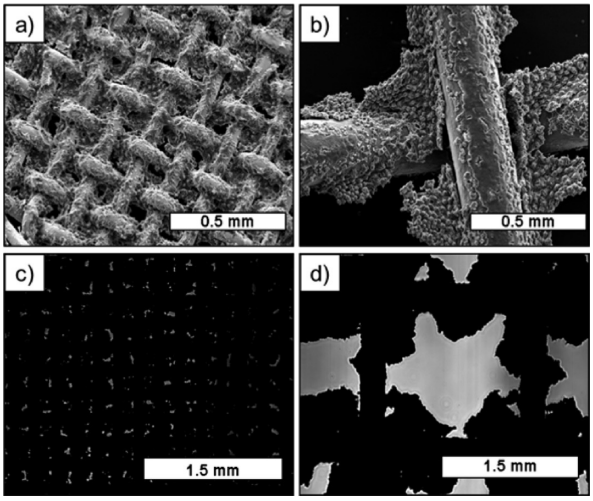

Figure 3. Optical images and SEM micrographs of two additional mesh sizes coated in a 60 mg mL^{-1} solution. (a) SEM micrograph of a 100 μm mesh. (b) SEM micrograph of a 1500 μm mesh (c) Optical image of the same 100 μm mesh (d) Optical image of the same 1500 μm mesh.

Surface Roughness and Liquid Contact Angles. At the higher concentrations (30 and 60 mg mL^{-1}), the LDPE coated on the stainless steel mesh was visibly white in color, which is different from common, transparent solid LDPE. This could be explained by a highly porous LDPE coating, which would scatter light and cause the surface to appear white. Higher-magnification SEM micrographs (Figure 4) confirm this observation, indicating the presence of sub-micrometer structures in the LDPE coating. DSC analysis of the 220 μm mesh coated with various concentrations indicated that the coated LDPE is about 20% crystalline (see the Supporting Information for more details on the DSC analysis). Thus, the roughness may have been caused by evaporating the xylene quickly in the well ventilated fume hood, forming amorphous LDPE with small channels for xylene evaporation. This fast evaporation created micro- and nano-structures that were visible at all concentrations (see the Supporting Information).

The roughness of the coatings on the 220 μm mesh was quantified using both atomic force microscopy (AFM) and SEM. The AFM could only probe the highest, most horizontal portions of the coated meshes, since the length of the probe (7 μm) was much smaller than the inherent topography of the woven mesh, and the curvature of the wires would artificially skew the roughness ratio based on sampling location. These sections tended to be free of microstructures (e.g. Figure 2d); thus, any changes would reflect the characteristics of a baseline coating. To compliment this measurement, a number distribution of pixel greyscale values was generated from the high magnification SEM images (e.g. Figure 4). The standard deviation of these distributions is known as the SEM index, and has been shown to correlate with surface roughness.[21] These values are reported in Table 3.

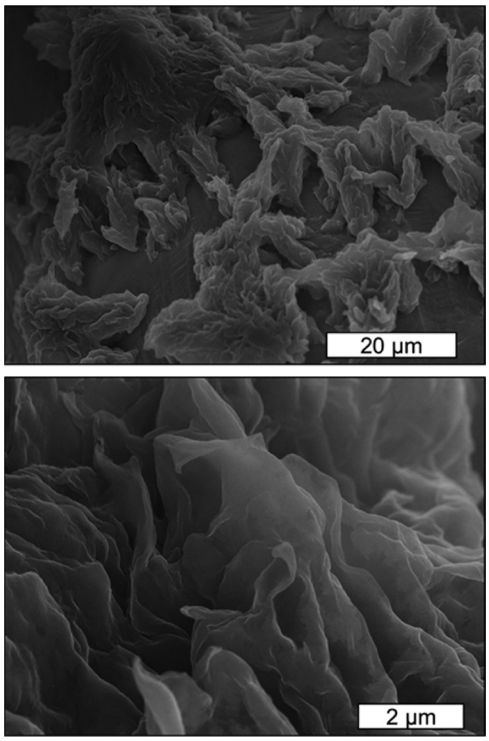

Figure 4. High-magnification SEM micrographs of a 220 μm mesh coated with a 60 mg mL^{-1} LDPE-xylene solution. The LDPE coating exhibits both micro- and nanoscale structures.

Table 3. Roughness Parameters of the 220 μm Mesh with Various Coatings

coating concentration (mg/mL)	AFM roughness ratio of raised wire surfaces	SEM index
uncoated	1.005 ± 0.003	6.58
15	1.053 ± 0.003	18.6
30	1.077 ± 0.005	21.6
60	1.096 ± 0.006	24.1

Despite not being able to directly measure the roughness ratio of the thickest sections of the LDPE coating, the SEM index clearly shows an increase in surface roughness with LDPE coating concentration. The AFM results indicate that although the uppermost surfaces of the steel mesh only become coated with LDPE that is smoother than other sections, it still becomes rougher as the concentration of the coating solution is increased. Overall, the combination of mesh openings on the order of 100 micrometers, surface structures on the order of 5 micrometers, and sub-micrometer features within the microstructures suggests complex wetting behavior that can be further quantified through contact angle analysis.

While the surface chemistry of smooth LDPE alone makes it hydrophobic (water contact angle of about 100°[22]), a highly porous and/or rough surface will enhance its hydrophobicity. The apparent contact angle on a rough surface that consists of

two substances (in this case, LDPE and air within the mesh openings or trapped between the water and LDPE) can be found by combining the Wenzel[23] and Cassie−Baxter[24] equations into[25]

$$\cos\theta^* = f r_f \cos\theta + f - 1 \quad (1)$$

where θ^* is the apparent water contact angle of the composite surface, f is the area fraction of the projection of the LDPE in contact with the liquid, r_f is the roughness ratio of the part of the LDPE surface that is wet by the liquid (ratio of actual surface area to apparent surface area), and θ is the contact angle of water on a smooth LDPE surface. Note that increasing the roughness ratio for a hydrophobic surface ($\theta > 90°$) increases the apparent contact angle, and decreases the apparent contact angle for hydrophilic surfaces. In addition, for either type of surface, decreasing the fraction of solid in contact with the liquid will increase the apparent contact angle, as the contact angle of any liquid with air is assumed to be 180°.[26] This fraction of air affects the value of f through both the openings in the mesh, and any partial wetting of the LDPE surface resulting from submicrometer structures.

The contact angle of a 10 μL drop of water was measured for each of the coated mesh surfaces (Figure 5). As expected given

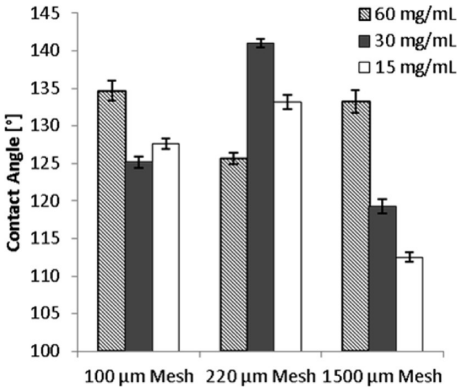

Figure 5. Measured water contact angles on stainless steel meshes coated in various concentrations of LDPE-xylene solutions. Mesh size refers to the width of the uncoated openings. Both the coating thickness and roughness increased with solution concentration.

the existence of openings in the mesh beneath the drops (decreasing the value of f in eq 3), all of the coated meshes exhibited contact angles higher than that of a flat LDPE surface (about 100°). However, the effect of increasing the coating concentration was less straightforward. The 1500 μm mesh contact angle exhibited an inverse relationship with the coating concentration, while the same relationship was non-monotonic for the 100 and 220 μm meshes.

The water contact angle results can be partially explained by the competing parameters f and r_f in eq 3. As the concentration of the LDPE-xylene solution increased, the LDPE coating grew thicker and filled more of the area between the wires. This would increase the area fraction of the projection of LDPE in contact with the liquid (f), and decrease the apparent contact angle. However, SEM micrographs and AFM measurements revealed that higher concentrations also produced rougher coatings, which would increase the value of r_f and increase the apparent contact angle. Furthermore, increasing the roughness will increase f as well, since the submicrometer features on the LDPE coatings will likely not become fully wetted by the liquid. Thus, increasing the coating thickness causes both f and r_f to increase, and it is not clear which factor dominates a priori. For the 100 and 200 μm meshes, it appears that the dominating parameter switched as the coating thickened, whereas it is likely that the relative increase in f dominated for the largest mesh. However, without the ability to directly measure either parameter, quantitatively decoupling these competing effects is difficult. Nevertheless, the variation in apparent contact angle and the visibly irregular microstructures strongly suggest that microscale roughness plays a significant role in determining the hydrophobic properties of these LDPE-coated meshes.

In addition to its hydrophobicity, we observed that the LDPE-coated stainless steel mesh was oleophilic, with apparent contact angles for the canola, olive, castor, and crude oils of about 0°. We also observed that the LDPE-coated mesh has a contact angle of 0° for ethanol and dichloromethane. After rinsing with dichloromethane, SEM micrographs revealed no deterioration of the coating or microstructures (see the Supporting Information for comparison), demonstrating that the coated mesh can be cleaned with organic solvents and reused. Therefore, the hydrophobic and oleophilic properties make the LDPE-coated stainless steel mesh a suitable candidate for water−oil separation.

After the oil contact angle experiments, it was observed that the area of mesh which came in contact with the oil was slightly darker in color than other portions. This discoloration indicates persistent wetting by the oil, which was confirmed with SEM micrographs (see the Supporting Information). Contact angles for the 220 μm mesh with a 60 mg mL^{-1} coating wetted with each type of oil were between 105 and 110°. The oil displaced any trapped air associated with the rough LDPE surface, and consequently attenuated the roughness effect. That is, the wetted surface becomes a composite interface of oil and LDPE, not air and LDPE as assumed in eq 1. Because of the relatively similar intermolecular forces of LDPE and the experimental oils, the wetted mesh behaved more like a homogeneous LDPE surface than a composite surface. Future separation applications of rough surfaces in the presence of a wetting fluid should account for the attenuation of the roughness effect with respect to water breakthrough pressure.

Breakthrough Pressure of Water. When considering the use of the LDPE-coated mesh as part of an oil spill remediation device, the possibility of submergence requires knowledge of the pressure needed to force water through the hydrophobic mesh. The classical Laplace equation describes the static pressure difference across the water-air meniscus that forms within each capillary-like opening in the coated mesh

$$\Delta P = \gamma_{LV}\left(\frac{1}{R_1} + \frac{1}{R_2}\right) \quad (2)$$

where γ_{LV} is the air-water surface tension, and R_1 and R_2 are the two orthogonal radii of curvature of the interface. Water will break through the mesh when the local water pressure becomes greater in magnitude than the capillary pressure within the mesh openings.

To apply eq 2, we idealized the mesh openings to be similar to the hole of a torus. This idealization is an attempt to capture the effect of both the geometry of the woven steel wires, and the shape of the opening after an LDPE coating is applied. The cross-section of such a shape is shown in Figure 6. As an additional simplification, the meniscus is assumed to take the shape of an axisymmetric spherical cap, which reduces the two

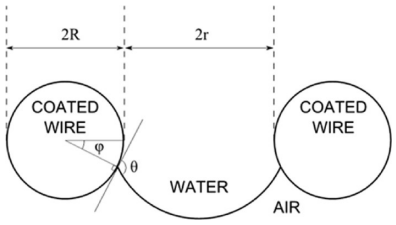

Figure 6. Cross-section of the water meniscus suspended within an idealized coated mesh opening. As the water column height above the meniscus changes, the contact point (located by the angle from the horizontal, φ) moves up or down the surface of the wire, while maintaining a constant contact angle θ relative to the local tangent.

orthogonal radii of curvature to a single, mean radius of curvature. The meniscus, oriented to oppose the hydrostatic pressure of the water, must maintain a constant contact angle relative to the tangent of the surface.

Liu and Lange[27] used a similar approach to describe the pressure required to transition to a fully wetted state from a Cassie–Baxter state on a flat surface with a regular array of spherical protrusions. By adapting their capillary pressure equation for our proposed model, and setting the pressure equal to the hydrostatic pressure of water, the depth of water h required to break through the LDPE-coated mesh was estimated to be

$$h = \frac{-2\gamma_{LV}\cos(\theta + \varphi)}{\rho g(r + R[1 - \cos\varphi])} \quad (3)$$

where ρ is the density of water, g is the gravitational acceleration, θ is the local water contact angle, and φ is the angle the three-phase contact line makes with the horizontal. When φ is equal to zero, eq 3 is reduced to the common equation for finding the height of a liquid in a capillary tube. As the contact line moves down the pore, the term $R[1 - \cos\varphi]$ captures the widening of the pore, while the term $\cos(\theta + \varphi)$ represents the apparent contact angle of the meniscus, as seen relative to the vertical in Figure 5. Since these two factors are in the denominator and numerator, respectively, they compete against one another as φ increases from zero to $\pi - \theta$. Thus, eq 3 has some maximum value of h as a function of φ, which represents the maximum depth a mesh with given values of r, R, and θ can withstand before water intrusion occurs.

Strictly speaking, the local contact angle θ must take into account local roughness and fractional wetted area, neither of which are known. The model assumes the local contact angle is equal to that of a smooth LDPE surface. The maximum height is relatively insensitive to θ compared to r and R, especially given the large uncertainties present in the pore dimensions (see Table 2). As an example, for the 220 μm mesh with a 60 mg mL^{-1} coating, it would take a local contact angle of 133° to match the error introduced by the moderate variance in the pore radius. This assumption allows us to find the mean radius of curvature using the radius of the mesh opening and the contact angle between water and the LDPE surface.

The LDPE-coated meshes were tested to determine the breakthrough depth, and compared to results predicted by eq 3 using the average pore dimensions and a local contact angle of 100°, representing smooth LDPE (Figure 7). Water began to percolate through the smallest mesh at a depth of 29 cm, compared to a predicted depth of 88 cm. The predicted depth for the medium mesh, 15 cm, matched the observed depth. The largest mesh only held back 1 cm of water, compared to a

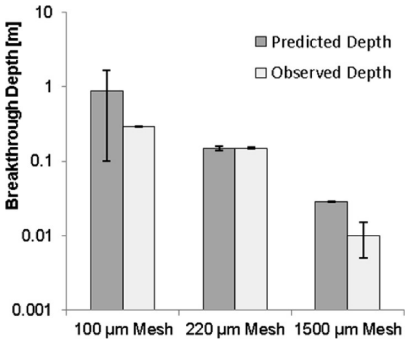

Figure 7. Depths at which water percolated through meshes coated with a 60 mg mL^{-1} LDPE-xylene solution compared to the depths predicted by eq 3. The error bars represent propagation of the mean pore area standard deviation for the predicted depths, and experimental precision for the observed depths.

prediction of 3 cm. Propagating the standard deviation of the mean pore area (as exhibited by the error bars) reveals that the observed depths agree with the predicted depths to within quantifiable uncertainty, excluding the largest mesh. For that particular case, the discrepancy can be attributed to the small, non-circular pore openings (Figure 3c), which would support a highly non-ideal meniscus. Given such large and irregular morphology, eq 3 will be a poor predictor of the breakthrough depth. However, the expression serves as a surprisingly good predictor in the other cases, given the heterogeneity seen in the pore size distribution and morphology. In addition, the experimental results confirm an inverse relationship between pore size and water breakthrough depth, and indicate that the mesh openings must be on the order of hundreds of micrometers or smaller to withstand depths of more than a few centimeters. As a final note, the above model indicates that the coated wire thickness plays a role in determining the water breakthrough depth, which is not accounted for by simply assuming the opening is a capillary tube. Such a formulation provides an additional design parameter (besides the pore radius) which can be used to improve the breakthrough depth.

Continuous Recovery of "Spilled" Oil Floating on Water. Finally, to assess the rate of oil recovery using hydrophobic meshes, we constructed a bench-scale oil collection unit by integrating the LDPE-coated meshes into a continuous pumping system (Figure 1). By immersing this unit into various oils floating on water, we could observe and quantify the rates of oil recoveries as a function of mesh size and oil viscosity.

First, using three cooking oils that exhibit viscosities that vary by more than a factor of 10 (Table 1), we tested the dependency of oil recovery rates on oil viscosity (Figure 8). For the less viscous canola and olive oils, 25 mL of oil were recovered in a matter of minutes. The more viscous castor oil required about 2 h to fully recover the same volume. Next, we tested the effect of mesh size using a single oil, Southern Louisiana crude, and seawater from Boston Harbor. Most of the initial 25 mL of oil was recovered in a few minutes with the large and medium mesh sizes (Figure 9). In contrast, the finest mesh size still had collected only about 70% of the same volume after 2 h.

However, we noted that much of the requisite time may have involved the slow flow of the oil across the surface of the water (e.g., see picture on right in Figure 1). Building from this hypothesis, we determined that there were three possible

dx.doi.org/10.1021/am302338x | ACS Appl. Mater. Interfaces 2013, 5, 774–781

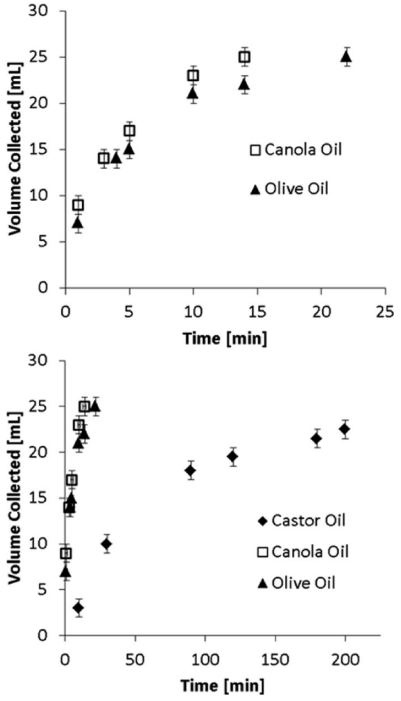

Figure 8. Recovery of a simulated 25 mL oil spill by a collection system for different common oils. The top panel shows results at short times (<25 min) and the bottom panel shows the complete results over a few hours, including the highly viscous castor oil. A 220 μm mesh coated in a 60 mg mL^{-1} LDPE-xylene solution was used each time.

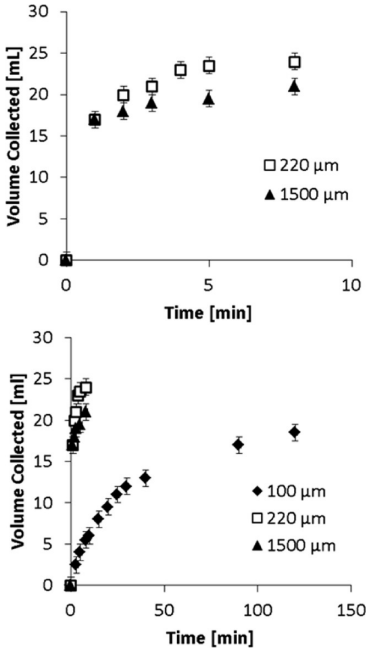

Figure 9. Results of oil spill recovery tests of 25 mL of Southern Louisiana crude oil floating on Boston Harbor seawater with the collection system equipped with varying mesh sizes. The listed mesh sizes refer to the uncoated opening widths; each mesh was coated in a 60 mg mL^{-1} LDPE-xylene solution before use. The top panel shows results for the first 10 min and bottom panel shows the same results over 2 h.

transport mechanisms that could limit the observed oil flow rate. The first is the rate at which oil spreads across the surface of the water to arrive at the surface of the hydrophobic mesh. Since the supply of spilled oil in the beaker was not refreshed, the oil layer thinned as it was collected and pumped away, which decreased the already meager head pressure (<100× capillary pressure) driving oil flow to the mesh. The second mechanism is the pumping of oil away from the inside of the collector. The pump was always run at a high enough rate to ensure that the inner face of the LDPE was never submerged in oil, thus maintaining a constant atmospheric pressure on the downstream side of the mesh. The final and most relevant transport mechanism is the flow through the LDPE-coated mesh. Assuming that it is largely driven by capillary action, the Washburn equation[28] can be applied to estimate the flux

$$q = \frac{1}{4(R+r)^2} \cdot \frac{\pi r^3 \gamma_{LV}}{4\eta(2R)} \quad (4)$$

where q is the volumetric flow rate of oil per unit area of mesh, γ_{LV} is the liquid-vapor surface tension of the oil, and η is the dynamic viscosity of the oil. In deriving this equation, the hydrostatic head of the oil is neglected, the oil is assumed to fully wet the LDPE coating, the capillary length is approximated by twice the coated wire radius ($2R$), and the term $1/4(R + r)^2$ represents the number of pores per unit area of mesh (the inverse is the surface area occupied by a single mesh opening and surrounding wire).

Given that a thinning layer of oil would decrease the oil-mesh contact area, A, and that the rate of oil spreading was observed to limit the flow throughout most of the experiment, the initial rate of oil uptake is the only measured flux which would be controlled by capillary action. Table 4 contains the initial area of mesh in contact with the oil (between 1 and 4 cm^2), and compares the initial fluxes observed with the fluxes predicted by eq 4 based on the previously calculated values of r and R.

Table 4. Comparison of the Observed and Predicted Initial Flow Rates of Oil

	observed initial flux (L/(s m^2))	predicted initial flux[c] (L/(s m^2))	initial oil-mesh contact area (cm^2)
mesh[a]			
100 μm	0.034 ± 0.003	0.013 ± 0.022	3.88 ± 0.02
220 μm	2.3 ± 0.2	0.9 ± 0.3	1.22 ± 0.01
1500 μm	20 ± 7	295 ± 101	2.43 ± 0.01
oil[b]			
castor	0.046 ± 0.004	0.076 ± 0.017	1.22 ± 0.01
olive	0.96 ± 0.17	0.78 ± 0.19	1.22 ± 0.01
canola	1.23 ± 0.19	0.82 ± 0.20	1.22 ± 0.01

[a]Size indicates uncoated width opening. All meshes were coated with a 60 mg mL^{-1} LDPE-xylene solution. Southern Louisiana crude oil in seawater was used each time. [b]Each oil was run through the same 220 μm mesh coated with a 60 mg mL^{-1} LDPE-xylene solution, which was cleaned with dichloromethane and air-dried between uses. [c]Error represents propagation of mean pore area standard deviation.

The Washburn equation demonstrated suitable predictions of the initial flux when the oil viscosity was varied for a single mesh. The experimental and calculated uncertainties overlap, or nearly so, and the observed initial flux rate exhibited an inverse relationship with viscosity as expected. However, when the mesh was varied using the same oil, significant deviations were observed. For the largest mesh, the initial flux was smaller than expected by about a factor of 20. Because both the 220 and

1500 μm meshes had the same initial flow rate, it is possible that the rate-limiting transport mechanism was not capillary action through the mesh, but either the transport of oil across the water surface, or the maximum pumping rate from the collector. The other meshes demonstrated fluxes about 3 times higher than expected, but given the large non-numeric uncertainties generated from calculating a mean effective pore radius and wire diameter, this is not an unreasonable result. And, as seen in Figure 9, overall there was an inverse relationship between flux and pore size, in agreement with eq 4. This result signifies a trade-off between oil flow and water intrusion resistance as pore size decreases. Future applications of an LDPE-coated mesh for oil spill remediation must balance these competing factors in order to achieve effective field implementation.

Finally, for each experiment, the oil permeate was collected and analyzed for water content by gravimetric desiccation. In all cases, the permeate contained less the 1% water by mass, which was the experimental detection limit. Despite being in contact with both oil and water during the experiment, the LDPE-coated meshes were able to successfully reject nearly all of the free-phase water.

CONCLUSION

Rough LDPE was successfully coated on stainless steel meshes in a manner in which the thickness of LDPE coating, and thus the size of the openings, could be tuned. The resultant LDPE-coated mesh was hydrophobic and oleophilic, as demonstrated by contact angle measurements and qualitative testing. A bench-top device was fabricated to demonstrate the efficacy of such an oil recovery device and to quantify the factors governing the ability of the mesh to separate oil and water. Our results suggested the device could work well on a variety of oil viscosities, with flow rate inversely related to viscosity. In addition, decreasing pore size was found to improve the water intrusion depth, but decreased the rate of oil recovery, indicating the existence of an optimal opening size for given field conditions and performance requirements. An expression was developed that accurately predicted the depth at which water intrusion occurred; and taken together with our approach for anticipating the oil uptake rate, one can envision optimizing mesh sizes and coating thicknesses to achieve recovery of spilled oil. Future efforts will entail testing such a hydrophobic mesh device in the field.

ASSOCIATED CONTENT

Supporting Information

Additional high-magnification SEM micrographs of the coated surfaces, optical microscopy images, AFM micrographs, DSC results, a description of separation experiments, and a video demonstrating the recovery of spilt oil have been provided. This material is available free of charge via the Internet at http://pubs.acs.org.

AUTHOR INFORMATION

Corresponding Author

*E-mail: pmgschwe@mit.edu.

Author Contributions

§These authors contributed equally to this work

Notes

The authors declare the following competing financial interest(s): This project was supported by funding from Eni S.p.A..

ACKNOWLEDGMENTS

The authors thank Eni S.p.A for their generous support of this research. This work made use of the MRSEC Shared Experimental Facilities at MIT, supported by the National Science Foundation under award number DMR-08-19762. In addition, the authors thank Prof. Roman Stocker for the use of his microscopes, and Jennifer N. Apell for editing.

REFERENCES

(1) Vanem, E.; Endresen, Ø.; Skjong, R. *Reliab. Eng. Syst. Saf.* **2008**, *93*, 1354−1368.
(2) Camilli, R.; Di Iorio, D.; Bowen, A.; Reddy, C. M.; Techet, A. H.; Yoerger, D. R.; Whitcomb, L. L.; Seewald, J. S.; Sylva, S. P.; Fenwick. *Proc. Natl. Acad. Sci. U. S. A.* **2011**, *109* (50), 20260−20267.
(3) Ventikos, N. P.; Vergetis, E.; Psaraftis, H. N.; Triantafyllou, G. *J. Hazard. Mater.* **2004**, *107*, 51−58.
(4) Dave, D.; Ghaly, A. E. *Am. J. Environ. Sci.* **2011**, *7*, 423−440.
(5) Adebajo, M.O.; Frost, R.L.; Kloprogge, J.T.; Carmody, O.; Kokot, S. *J. Porous Mater.* **2003**, *10*, 159−170.
(6) Feng, L.; Zhang, Z.; Mai, Z.; Ma, Y.; Liu, B.; Jiang, L.; Zhu, D. *Angew. Chem., Int. Ed.* **2004**, *43*, 2012−2014.
(7) Tu, C.; Tsai, C.; Wang, C.; Kuo, S.; Chang, F. *Macromol. Rapid Commun.* **2007**, *28*, 2262−2266.
(8) Wu, J.; Chen, J.; Qasim, K.; Xia, J.; Lei, W.; Wang, B. *J. Chem. Technol. Biotechnol.* **2012**, *87*, 427−430.
(9) Lee, C.; Baik, S. *Carbon* **2010**, *48*, 2192−2197.
(10) Lee, C.; Johnson, N.; Drelich, J.; Yap, Y. K. *Carbon* **2011**, *49*, 669−676.
(11) Li, M.; Xu, J.; Lu, Q. *J. Mater. Chem.* **2007**, *17*, 4772−4776.
(12) Wang, C.; Yao, T.; Wu, J.; Ma, C.; Fan, Z.; Wang, Z.; Cheng, Y.; Lin, Q.; Yang, B. *ACS Appl. Mater. Interfaces* **2009**, *11*, 2613−2617.
(13) Pan, Q.; Wang, M.; Wang, H. *Appl. Surf. Sci.* **2008**, *254*, 6002−6006.
(14) Wang, S.; Song, Y.; Jiang, L. *Nanotechnology* **2007**, *18*, 015103.
(15) Xue, Z.; Wang, S.; Lin, L.; Chen, L.; Liu, M.; Feng, L.; Jiang, L. *Adv. Mater.* **2011**, *23*, 4270−4273.
(16) Howarter, J. A.; Youngblood, J. P. *J. Colloid Interface Sci.* **2009**, *329*, 127−132.
(17) Yang, J.; Zhang, Z.; Xu, X.; Zhu, X.; Men, X.; Zhou, X. *J. Mater. Chem.* **2012**, *22*, 2834−2837.
(18) Yuan, J.; Liu, X.; Akbulut, O.; Hu, J.; Suib, S. L.; Kong, J.; Stellacci, F. *Nat. Nanotechnol.* **2008**, *3*, 332−336.
(19) Liu, K.; Jiang, L. *Nanoscale* **2011**, *3*, 825−838.
(20) Stalder, A. F.; Melchior, T.; Müller, M.; Sage, D.; Blu, T.; Unser, M. *Colloids Surf., A* **2010**, *364*, 72−81.
(21) Banerjee, S.; Yang, R.; Courchene, C. E. *Ind. Eng. Chem. Res.* **2009**, *48*, 4322−4325.
(22) Lu, X.; Zhang, C.; Han, Y. *Macromol. Rapid Commun.* **2004**, *25*, 1606−1610.
(23) Wenzel, R. N. *Ind. Eng. Chem.* **1936**, *28*, 988−994.
(24) Cassie, A. B. D.; Baxter, S. *Trans. Faraday Soc.* **1944**, *40*, 546−551.
(25) Marmur, A. *Langmuir* **2003**, *19*, 8343−8348.
(26) Quéré, D. *Physica A* **2002**, *313*, 32−46.
(27) Liu, B.; Lange, F. F. *J. Colloid Interface Sci.* **2006**, *298*, 899−909.
(28) Washburn, E. W. *Phys. Rev.* **1921**, *17*, 273−283.